Photodissociation of O2 in the Herzberg continuum. II. Calculation of fragment polarization and angular distribution

Mirjam C. G. N. van Vroonhoven and Gerrit C. Groenenboom

Citation: J. Chem. Phys. **116**, 1965 (2002); doi: 10.1063/1.1427715
View online: http://dx.doi.org/10.1063/1.1427715
View Table of Contents: http://jcp.aip.org/resource/1/JCPSA6/v116/i5
Published by the AIP Publishing LLC.

Photodissociation of O_2 in the Herzberg continuum. II. Calculation of fragment polarization and angular distribution

Mirjam C. G. N. van Vroonhoven and Gerrit C. Groenenboom[a)]
Institute of Theoretical Chemistry, University of Nijmegen, Toernooiveld 1, 6525 ED Nijmegen, The Netherlands

(Received 24 July 2001; accepted 23 October 2001)

Parallel and perpendicular components of the Herzberg I, II, and III transitions contribute to the photodissociation of O_2 in the Herzberg continuum. The photodissociation dynamics determines the $O(^3P_j)$, $j=0,1$, and 2 atomic fine-structure branching ratios and angular distributions, which were determined in ion imaging experiments at $\lambda=236$, 226, and 204 nm by Buijsse *et al.* [J. Chem. Phys. **108**, 7229 (1998)]. In the preceding paper we presented potential energy curves for all eight ungerade O_2 states that correlate with the $O(^3P)+O(^3P)$ dissociation limit, and the R-dependent spin–orbit and the nonadiabatic radial derivative couplings between these states. Here, we employ these potentials and couplings in a semiclassical calculation of the fine-structure branching ratios, atomic polarizations, and fine-structure resolved anisotropy parameters. We discuss the adiabaticity of the dissociation by comparing the results with adiabatic and diabatic models. The $O(^3P_j)$ 2+1 REMPI detection scheme used in the experiment is sensitive to the polarization of the atomic fragments. We predict an important effect of the polarization on the anisotropy of the $j=1$ and $j=2$ ion images at low energies ($\lambda>236$ nm). The agreement between the semiclassical calculations and experiment is reasonable, possible explanations for the remaining differences are discussed. [DOI: 10.1063/1.1427715]

I. INTRODUCTION

The photodissociation of molecules into open-shell fragments is interesting because generally multiple coupled electronic states are involved. For nonsinglet state fragments the (nonadiabatic) couplings determine the fine-structure branching ratios. This has been studied in detail for the relatively simple HCl and OH molecules.[1,2] The photodissociation of O_2 in the Herzberg continuum is complicated since already in the excitation step several electronically excited states are involved. Both parallel and perpendicular electronic transitions contribute. This is reflected in the angular distribution of the photofragments, which was studied by Buijsse *et al.*[3] with the velocity mapped ion imaging technique.[4] In the experiment O_2 was cooled to 5–10 K in a molecular beam, and photodissociated with a linearly polarized laser at 236, 226, and 204 nm. At these energies only the three fine-structure components of the ground state $O(^3P_{j=2,1,0})$ atoms can be produced. State selective detection of the atoms was achieved by (2+1) resonance enhanced multiphoton ionization (REMPI) of the $O(^3P_j)$ states. The angular distribution of the $O(^3P_j)$ photofragments can be expressed as $[1+\beta_j(E)P_2(\cos\theta)]$, where P_2 is the second order Legendre polynomial, θ is the angle between the polarization of the dissociation laser and the recoil velocity, and $\beta_j(E)$ is the fine-structure resolved and energy dependent anisotropy parameter. The observed ion image actually corresponds to the distribution of the ions. This may be different from the distribution of the atoms when the atoms are polarized, because the ionization efficiency depends on the angle between the recoil velocity and the polarization of the detection laser. This angle is equal to θ because the laser polarizations were taken parallel to each other. In the case of direct dissociation, which is appropriate in this case, the fine-structure averaged β parameter is fully determined by the parallel/perpendicular character of the initial electronic excitation.

The fine-structure dependent anisotropy parameters $\beta_j(E)$ may differ for $j=2$, 1, and 0, if the fine-structure branching ratios of the electronic states reached via a parallel transition differ from those reached via perpendicular transitions. In the adiabatic limit all electronic states involved correlate with the $O(^3P_2)+O(^3P_2)$ limit. It turns out that even at 236 nm the dissociation is not fully adiabatic and hence the experiment contains information on the nonadiabatic coupling between the electronic states.

Apart from the initially excited Herzberg states ($A\ ^3\Sigma_u^+$, $c\ ^1\Sigma_u^-$, and $A'\ ^3\Delta_u$) there are five other ungerade states ($1\ ^1\Pi_u$, $1\ ^3\Pi_u$, $2\ ^3\Sigma_u^+$, $1\ ^5\Pi_u$, and $1\ ^5\Sigma_u^-$) that correlate with the $O(^3P)+O(^3P)$ dissociation limit and are involved in the dissociation dynamics through spin–orbit interactions (in the long range). Furthermore, the $A\ ^3\Sigma_u^+$ and $2\ ^3\Sigma_u^+$ states are coupled through the radial derivative coupling $g_{2,A}(R)=\langle 2\ ^3\Sigma_u^+|\partial/\partial R|A\ ^3\Sigma_u^+\rangle$ which arises from the nonseparability of the electronic and nuclear motion. In the preceding paper,[5] which we will refer to as paper I, we presented high quality *ab initio* calculations of the potential energy curves and R-dependent spin–orbit couplings for all eight electronic states, as well as $g_{2,A}(R)$. In the present paper we employ these *ab initio* results in a semiclassical calculation of the energy dependent fine-structure branching

a)Author to whom correspondence should be addressed. Electronic mail: gerritg@theochem.kun.nl

ratios for the three Herzberg states. We also compute the energy dependent atomic alignment. By taking into account the experimental values in Ref. 3 for the parallel and perpendicular branching ratios of the Herzberg transitions we calculate the anisotropy parameters for the ions, which we compare to the experimental results of Buijsse.[3]

In the present work we neglect the possible effects of coherent excitation of the Herzberg states and Coriolis coupling. Such effects may be important for photodissociation of O_2 in a well-defined initial quantum state, for which no experimental data is available yet. Also, properly describing these effects may require a full coupled-channels quantum treatment. Thus, the present semiclassical study should be considered as the first step beyond the adiabatic and diabatic models. Note that a full quantum treatment would also require knowledge of the radial second derivative nonadiabatic couplings and a complete model of the initial electronic excitation, rather than just the electronic excitation branching ratios.

The outline of this paper is as follows. In the next section (Sec. II) we present the theoretical framework of this paper. We describe the construction of diabatic and adiabatic models (Sec. II A), the semiclassical calculation and our extended diabatic model, which includes the nonadiabatic radial derivative coupling (Sec. II B), and the procedure to calculate atomic fine-structure branching ratios, alignment and ion images from the dynamics results (Sec. II C). In Sec. III we discuss the results of the dynamics calculations, and the resulting fragment branching ratios and alignments. We present our conclusions in Sec. IV. The derivation of the angular REMPI detection sensitivity is given in the Appendix.

II. THEORY

A. Adiabatic and diabatic model

The construction of adiabatic and diabatic models to describe the fine-structure branching in diatomic molecules is well established.[6,7] First, we partition the total electronic Hamiltonian

$$\hat{H}(R)=\hat{H}_{\mathrm{coul}}(R)+\hat{H}_{\mathrm{SO}}(R), \tag{1}$$

where $\hat{H}_{\mathrm{coul}}(R)$ is the nonrelativistic electronic Hamiltonian in the clamped nuclei approximation, $\hat{H}_{\mathrm{SO}}(R)$ is the (Breit–Pauli) spin–orbit operator and R is the internuclear separation. In the region where the initial photoexcitation occurs ($R=R_a$) we assume that the eigenfunctions of $\hat{H}_{\mathrm{coul}}$ are a good first order approximation to the eigenfunctions of the full electronic Hamiltonian and $\hat{H}_{\mathrm{SO}}$ gives a small perturbation. The choice of R_a is not critical, provided that the adiabatic Born–Oppenheimer (ABO) potentials, i.e., the eigenvalues of $\hat{H}_{\mathrm{coul}}$, are well separated in this region. We take $R_a=2.85\ a_0$. Adiabatic dissociation with respect to $\hat{H}_{\mathrm{coul}}$ implies that the ith electronic eigenstate of $\hat{H}_{\mathrm{coul}}(R_a)$ of a given symmetry evolves into the ith eigenstate of the same symmetry for $R\rightarrow\infty$. When, for a given symmetry, the eigenstates of $\hat{H}_{\mathrm{coul}}(\infty)$ are degenerate we define the asymptotic ABO eigenstates by considering the leading interatomic term of the multipole expansion of $\hat{H}_{\mathrm{coul}}$ at large R that lifts the degeneracy. We followed this procedure in paper I to arrive at the ABO states $|(L)\Lambda S\Sigma;R\rangle$, which are eigenstates of $\hat{H}_{\mathrm{coul}}(R)$ and where Λ, S, and Σ are (good) Hund's case (a) quantum numbers of the O_2 molecule. By considering the quadrupole–quadrupole interaction between the $O(^3P)$ fragments, we found that L, which is the asymptotic total orbital angular momentum, can be used to label the asymptotically degenerate $A\ ^3\Sigma_u^+(L=0)$ and $2\ ^3\Sigma_u^+(L=2)$ states for any R.

The ABO states are eigenfunctions of the electronic inversion operator[8] $\hat{\pi}$, with eigenvalues $(-1)^{L+S}$. Here we consider only ungerade states, so $L+S$ must be odd. We should also consider the inversion operator $\hat{i}$, which inverts both electronic and nuclear coordinates and which determines parity. For $\Omega\equiv\Lambda+\Sigma\neq 0$ states, however, this operator affects the rotational part of the wave function,[9] which we do not explicitly include in the present semiclassical formulation and so we may ignore it. For $\Omega=0$ states we have[9]

$$\hat{i}|(L)\Lambda S\Sigma;R\rangle=(-1)^{L+S}|(L)-\Lambda S-\Sigma;R\rangle. \tag{2}$$

Ungerade states with $\Lambda=\Sigma=0$ have an intrinsic parity of -1. For $\Lambda=-\Sigma\neq 0$ both odd and even parity states can be constructed. Note, however, that in the calculation of the spin–orbit coupling in paper I we employed the parity unadapted $^{3,5}\Pi_{u,0}(\Lambda=\pm 1)$ states. Asymptotically the ABO wave functions $|L\Lambda S\Sigma\rangle\equiv|(L)\Lambda S\Sigma;\infty\rangle$ can be expanded in product atomic wave functions

$$|L\Lambda S\Sigma\rangle=\sum_{\lambda_a\lambda_b\sigma_a\sigma_b}|l_a\lambda_a\rangle|s_a\sigma_a\rangle|l_b\lambda_b\rangle|s_b\sigma_b\rangle \times\langle l_a\lambda_a l_b\lambda_b|L\Lambda\rangle\langle s_a\sigma_a s_b\sigma_b|S\Sigma\rangle, \tag{3}$$

where a and b label the atoms and for $O(^3P)$ $l_a=l_b=s_a=s_b=1$ and $\lambda_a,\lambda_b,\sigma_a$, and σ_b are projections of the atomic angular momenta on the internuclear axis. The symbol $\langle a\alpha b\beta|c\gamma\rangle$ is a Clebsch–Gordan coefficient.

Since the spin–orbit interaction does not vanish asymptotically the analysis of the photofragments requires a recoupling to product atomic multiplet states $|j_a\omega_a j_b\omega_b\rangle\equiv|j_a\omega_a\rangle|j_b\omega_b\rangle$ where

$$|j_i\omega_i\rangle=\sum_{\lambda_i\sigma_i}|l_i\lambda_i\rangle|s_i\sigma_i\rangle\langle l_i\lambda_i s_i\sigma_i|j_i\omega_i\rangle;\quad i=a,b. \tag{4}$$

The transformation between the ABO states and the atomic eigenstates can be expressed as[9]

$$\langle j_a\omega_a j_b\omega_b|L\Lambda S\Sigma\rangle=\sum_{j'=0}^{4}\langle j_a\omega_a j_b\omega_b|j'\Omega\rangle \times\langle j'\Omega|L\Lambda S\Sigma\rangle\sqrt{[j_a][j_b][L][S]} \times\begin{Bmatrix} l_a & s_a & j_a\\ l_b & s_b & j_b\\ L & S & j'\end{Bmatrix}, \tag{5}$$

where $[X]\equiv 2X+1$ and the last factor is a 9-j symbol. This description of the photodissociation, correlating the ABO eigenstates $|(L)\Lambda S\Sigma;R_a\rangle$ of $\hat{H}_{\mathrm{coul}}(R_a)$ with asymptotic

ABO states $|L\Lambda S\Sigma\rangle$, and using Eq. (5) to transform the asymptotic ABO states into product atomic multiplet states, is called *diabatic* with respect to spin–orbit coupling, since the effect of the spin–orbit coupling is treated by the basis transformation. According to the Massey criterion[10] the diabatic or spin–orbit sudden limit is reached when the time for traversing the SO recoupling zone is small compared to $\hbar/\Delta E_{\mathrm{SO}}$, where ΔE_{SO} is the spin–orbit coupling. This is the high recoil velocity limit.

The low recoil velocity limit may be described by a model which is adiabatic with respect to the total electronic Hamiltonian $\hat{H}(R)$ [Eq. (1)]. In this case Λ and Σ are no longer good quantum numbers and the noncrossing rule only applies to states with the same value of Ω. Since $\hat{\pi}$ commutes with $\hat{H}_{\mathrm{SO}}$ as well as with $\hat{H}_{\mathrm{coul}}$ and the electronic states excited are ungerade, we construct *ungerade* coupled atomic states

$$|j_a\omega_a j_b\omega_b\rangle_u = 2^{-1/2}[|j_a\omega_a j_b\omega_b\rangle - |j_b\omega_b j_a\omega_a\rangle]. \quad (6)$$

Note that for dissociation into a $j_a=j_b$ channel we must have $\omega_a \neq \omega_b$. For $\omega_a+\omega_b=\Omega=0$ intrinsic parity adapted states may be constructed using

$$\hat{i}|j_a\omega_a j_b-\omega_a\rangle = (-1)^{j_a+j_b}|j_a-\omega_a j_b\omega_a\rangle. \quad (7)$$

From this it follows that ungerade $\Omega=0$ states with $j_a=j_b$ are odd parity states. The asymptotic energy of $|j_a\omega_a j_b\omega_b\rangle_u$ is $E_{j_a}+E_{j_b}$ with

$$E_j=(1/2)A[j(j+1)-l(l+1)-s(s+1)] = (1/2)A[j(j+1)-4], \quad (8)$$

where A is the atomic spin–orbit coupling constant[11] of -0.353 mE_h. These rules are sufficient to derive the adiabatic correlation diagram for the eight ungerade O_2 states as shown in Fig. 8 of Ref. 7. The Herzberg states all correlate adiabatically with the $j_a=j_b=2$ limit. For $\Omega=2,3$ [i.e., $A'\,^3\Delta_{u,2/3}$] we immediately find that the asymptotic states must be $|2220\rangle_u$ and $|2221\rangle_u$, respectively. However, for $\Omega=0^-$ there are two asymptotically degenerate states: $|222-2\rangle_{u^-}$ and $|212-1\rangle_{u^-}$, and for $\Omega=1$ we have $|222-1\rangle_u$ and $|2120\rangle_u$. In order to find the atomic polarization in the adiabatic model for the $\Omega=0^-$ states we must find the proper linear combination of $|222-2\rangle_{u^-}$ and $|212-1\rangle_{u^-}$ that correlates with the lowest lying $\Omega=0^-$ Herzberg state ($c\,^1\Sigma^-_{u,0^-}$). For $\Omega=1$ we must find the proper linear combination of $|222-1\rangle_u$ and $|2120\rangle_u$ that correlates with $A'\,^3\Delta_{u,1}$, the lowest lying $\Omega=1$ Herzberg state. Just as in the construction of the asymptotic ABO states we do this by diagonalizing the quadrupole–quadrupole interaction in the basis of degenerate states. The matrix elements ${}_u\langle j_a\omega_a j_b\omega_b|\hat{V}_5|j_a\omega'_a j_b\omega'_b\rangle_u$ are found by inserting the resolution of identity in the molecular basis, $\hat{I}=\Sigma_{L\Lambda S\Sigma}|L\Lambda S\Sigma\rangle\langle L\Lambda S\Sigma|$, twice ($\hat{V}_5=\hat{I}\hat{V}_5\hat{I}$). The transformation coefficients are given in Eq. (5) and the quadrupole–quadrupole matrix elements in the molecular basis are given in Eq. (9) in paper I. Following this procedure we obtained the complete adiabatic model for the Herzberg states as given in Table I.

TABLE I. Adiabatic correlation between molecular Herzberg states and product atomic states.

State	$\Sigma_i c_i\|j_a\omega_a j_b\omega_b\rangle_u$
$c\,^1\Sigma^-_{u,0^-}$	$0.525\,73\,\|2-222\rangle_u - 0.850\,65\,\|2-121\rangle_u$
$A\,^3\Sigma^+_{u,0^-}$	$0.850\,65\,\|2-222\rangle_u + 0.525\,73\,\|2-121\rangle_u$
$A'\,^3\Delta_{u,1}$	$-0.985\,87\,\|2-122\rangle_u + 0.167\,51\,\|2021\rangle_u$
$A\,^3\Sigma^+_{u,1}$	$0.167\,51\,\|2-122\rangle_u + 0.985\,87\,\|2021\rangle_u$
$A'\,^3\Delta_{u,2}$	$1.0\,\|2220\rangle_u$
$A'\,^3\Delta_{u,3}$	$1.0\,\|2122\rangle_u$

B. Semiclassical dynamics

The Massey criterion gives only a crude indication of the validity of the adiabatic or diabatic models for predicting branching ratios. It is even less clear whether the models can be used to predict fragment polarization. Furthermore, the diabatic model presented so far does not take into account the effect of the nonadiabatic radial derivative coupling between the $A\,^3\Sigma^+_u$ and $2\,^3\Sigma^+_u$ states, which should be important in the high energy limit. Finally, the SO coupling in the Franck–Condon region is not completely negligible. Thus, we performed semiclassical calculations to study the energy dependence of the photodissociation process. It is well established[12,13] that the semiclassical approximation is valid for a De Broglie wavelength $\lambda/a_0 \ll 2\pi$. For the energy range considered in the experiment we have $0.2a_0 \leqslant \lambda \leqslant 0.6a_0$.

In the present semiclassical study we neglect the possible effects of coherent excitation of the Herzberg states. At $R_a=2.85\,a_0$ we compute the eigenfunctions of the total electronic Hamiltonian

$$[\hat{H}(R_a)-E_{i\Omega}(R_a)]\Psi_{i\Omega}(R_a)=0, \quad (9)$$

where i labels the eigenstates, sorted on energy, within each Ω symmetry block. Near equilibrium geometry the energy ordering of the states is $c\,^1\Sigma^-_u$, $A'\,^3\Delta_u$, and $A\,^3\Sigma^+_u$. So for $\Omega=0$, $i=1$ and 2 correspond to $c\,^1\Sigma^-_u$ and $A\,^3\Sigma^+_u$, respectively. For $\Omega=1$ the lowest state ($i=1$) is $A'\,^3\Delta_u$, and $A\,^3\Sigma^+_u$ corresponds to $i=2$. For $\Omega=2$ and 3 we only have $A'\,^3\Delta_u$ initial states, these have $i=1$. See also Table II. We take each of the eigenfunctions corresponding to the Herzberg states as initial conditions for the semiclassical propagation. We expand $\Psi_{i\Omega}(R)$ in a basis of ABO states,

TABLE II. Herzberg excitation branching ratios $r_{i\Omega}$ and anisotropy parameters $\beta_{i\Omega}$ for the different molecular eigenstates ($i\Omega$) of the Herzberg transition. These depend on the excitation wavelength λ in nm. Given energy dependencies are linear fits from Fig. 7 of Ref. 3, and $\lambda' \equiv \lambda - 226$.

State	$(i,\|\Omega\|)$	$\beta_{i\Omega}$	$r_{i\Omega}$
$c\,^1\Sigma^-_{u,0^-}$	(1,0)	-1	$0.0228+3.439\times10^{-4}\lambda'$
$A'\,^3\Delta_{u,1}$	(1,1)	-1	$0.0223+3.356\times10^{-4}\lambda'$
$A'\,^3\Delta_{u,2}$	(1,2)	-1	$0.0334+5.034\times10^{-4}\lambda'$
$A'\,^3\Delta_{u,3}$	(1,3)	-1	$0.0005+7.5\times10^{-6}\lambda'$
$A\,^3\Sigma^+_{u,0^-}$	(2,0)	-1	$0.1883-6.822\times10^{-4}\lambda' + 5.67\times10^{-7}\lambda'^2$
$A\,^3\Sigma^+_{u,1}$	(2,1)	$1.2288 + 2.2589\times10^{-3}\lambda' - 2.1328\times10^{-6}\lambda'^2$	$0.7327-5.0779\times10^{-4}\lambda' - 5.67\times10^{-7}\lambda'^2$

$$\Psi_{i\Omega}(R)=\sum_{L\Lambda S\Sigma} c^{i\Omega}_{L\Lambda S\Sigma}(R)|(L)\Lambda S\Sigma;R\rangle. \tag{10}$$

Substituting this expression in the time-dependent Schrödinger equation while treating $R=R(t)$ as a classical coordinate and projecting with $\langle(L)\Lambda S\Sigma;R|$ gives the quantum-mechanical equations of motion

$$\begin{aligned} i\hbar\frac{\partial}{\partial t}\{c^{i\Omega}_{L\Lambda S\Sigma}[R(t)]\} &= \sum_{L'\Lambda'S'\Sigma'}\Bigg\{\langle(L)\Lambda S\Sigma;R|\hat{H}[R(t)]|(L')\Lambda'S'\Sigma';R\rangle \\ &\quad -i\hbar\frac{dR(t)}{dt}\left\langle(L)\Lambda S\Sigma;R\left|\frac{\partial}{\partial R}\right|(L')\Lambda'S'\Sigma';R\right\rangle\Bigg\} \\ &\quad \times c^{i\Omega}_{L'\Lambda'S'\Sigma'}[R(t)]. \end{aligned} \tag{11}$$

The diagonal elements of the first term on the right-hand side of this equation are equal to the ABO potentials $\epsilon_{L|\Lambda|S}(R)$ and the off-diagonal elements are the SO couplings. The radial derivative term arises from $\partial/\partial t=(dR/dt)\,(\partial/\partial R)$. This term only couples the $A\,^3\Sigma_u^+(|(0)01\Sigma;R\rangle)$ and $2\,^3\Sigma_u^+$ $(|(2)01\Sigma;R\rangle)$ states. The computation of the ABO potentials and the SO and $\partial/\partial R$ coupling is described in paper I. The nuclear motion $[R(t)]$ is governed by the classical Hamiltonian

$$H_{\rm cl}=\frac{p_R^2}{2\mu}+\langle\Psi[R(t)]|\hat{H}[R(t)]|\Psi[R(t)]\rangle, \tag{12}$$

where μ is the reduced mass of O_2 and p_R is the momentum conjugate to R. The classical equations of motion are

$$\frac{dR}{dt}=\frac{\partial H_{\rm cl}}{\partial p_R}=\frac{p_R}{\mu}, \tag{13}$$

$$\begin{aligned} \frac{dp_R}{dt}=-\frac{\partial H_{\rm cl}}{\partial R}&=-\sum_{L\Lambda S\Sigma}\sum_{L'\Lambda'S'\Sigma'} c^{i\Omega *}_{L\Lambda S\Sigma}[R(t)] \\ &\quad\times\left\langle L\Lambda S\Sigma\left|\frac{\partial\hat{H}}{\partial R}\right|L'\Lambda'S'\Sigma'\right\rangle \\ &\quad\times c^{i\Omega}_{L'\Lambda'S'\Sigma'}[R(t)]. \end{aligned} \tag{14}$$

The initial conditions for the electronic state $(i\Omega)$ are $R(0)=R_a$ and $p_R(0)=\sqrt{2\mu(E-E_{i\Omega})}$. The total energy is given by $E=h\nu-D_0+2E_{j=2}$, where ν is the frequency of the dissociation laser, $D_0=188.034$ mE_h is the dissociation energy[14] of the ground state $X\,^3\Sigma_g^-$ and $E_{j=2}=-0.3526$ mE_h is the energy of an $O(^3P_2)$ atom with respect to our zero point of energy, which is chosen such that $\epsilon_{L|\Lambda|S}(\infty)=0$. The semiclassical equations have been solved numerically using the MATLAB computer linear algebra system.[15]

In addition to the semiclassical calculations we will also present the results of an extended diabatic model. In this model we still assume that SO coupling is negligible, but we do take into account the radial derivative coupling. Hence one may also refer to this model as spin–orbit sudden. Only for the $A\,^3\Sigma_u^+$ state it deviates from the diabatic model presented above. For this state it amounts to expanding the wave function as

$$\Psi(R)=c_0(R)|(0)01\Sigma;R\rangle+c_2(R)|(2)01\Sigma;R\rangle \tag{15}$$

and solving the semiclassical equations for two states, without the SO coupling, and with the initial condition $c_0(R_a)=1;c_2(R_a)=0$. Thus Eq. (11) becomes

$$\begin{aligned} i\hbar\frac{\partial}{\partial t}\begin{bmatrix}c_0[R(t)]\\ c_2[R(t)]\end{bmatrix}&=\begin{bmatrix}\epsilon_{001}[R(t)] & i\hbar\dot{R}g_{2,A}[R(t)]\\ -i\hbar\dot{R}g_{2,A}[R(t)] & \epsilon_{201}[R(t)]\end{bmatrix} \\ &\quad\times\begin{bmatrix}c_0[R(t)]\\ c_2[R(t)]\end{bmatrix}. \end{aligned} \tag{16}$$

When $\dot{R}=dR/dt$ is negligible we find $|c_0(\infty)|=1$ and $c_2(\infty)=0$ and hence the model reduces to the simple diabatic model presented above. In the high energy limit the potentials are negligible compared to the coupling and we find $c_0(\infty)=\cos\phi$ and $c_2(\infty)=\sin\phi$ with

$$\phi=-\int_{R_a}^{\infty} g_{2,A}(R')dR'. \tag{17}$$

With the radial derivative coupling computed in paper I we find $\phi=33.74°$.

C. Ion image

The computation of the ion image requires the $O(^3P_j)$ fine-structure populations and polarizations.[16,17] These are obtained by expanding the electronic wave function at large $R=R_b$ (we take $R_b=15\ a_0$ in the semiclassical calculation) in the coupled atomic basis

$$\Psi_{i\Omega}(R_b)=\sum_{j_a\omega_a j_b\omega_b} c^{i\Omega}_{j_a\omega_a j_b\omega_b}(R_b)|j_a\omega_a j_b\omega_b\rangle. \tag{18}$$

The expansion coefficients are calculated using the recoupling matrix element given in Eq. (5),

$$c^{i\Omega}_{j_a\omega_a j_b\omega_b}(R_b)=\sum_{L\Lambda S\Sigma}\langle j_a\omega_a j_b\omega_b|L\Lambda S\Sigma\rangle c^{i\Omega}_{L\Lambda S\Sigma}(R_b). \tag{19}$$

The two-atom density matrix is defined by

$$\rho^{i\Omega}_{j_a\omega_a j_b\omega_b;j'_a\omega'_a j'_b\omega'_b}(R_b)=c^{i\Omega}_{j_a\omega_a j_b\omega_b}(c^{i\Omega}_{j'_a\omega'_a j'_b\omega'_b})^*. \tag{20}$$

A partial trace over the quantum numbers of atom b gives the reduced density matrix for atom a

$$\begin{aligned} &\rho^{i\Omega}_{j_a\omega_a;j'_a\omega'_a}(R_b) \\ &\quad=\sum_{j_b\omega_b j'_b\omega'_b}\rho^{i\Omega}_{j_a\omega_a j_b\omega_b;j'_a\omega'_a j'_b\omega'_b}(R_b)\,\delta_{j_b j'_b}\delta_{\omega_b\omega'_b}. \end{aligned} \tag{21}$$

Since atoms a and b are indistinguishable and we are only interested in relative intensities we may ignore atom b. Using $\omega_a+\omega_b=\Omega=\omega'_a+\omega'_b$ in Eq. (21) shows that $\rho^{i\Omega}_{j_a\omega_a;j'_a\omega'_a}(R_b)=0$ for $\omega_a\neq\omega'_a$. This is a direct consequence of ignoring coherence in the excitation of different Ω states.

The detection is fine-structure selective, hence the atomic products are described by a $j_a = j'_a = j$ block of the density matrix, which is diagonal

$$\rho^{i\Omega}_{j\omega;j\omega'}(R_b) = P^{i\Omega}_{j\omega}\delta_{\omega\omega'}. \tag{22}$$

The R_b dependence disappears when R_b is sufficiently large. The atomic fine-structure level populations are given by

$$P^{i\Omega}_j = \sum_\omega P^{i\Omega}_{j\omega}. \tag{23}$$

The polarizations of the $O(^3P_j)$ states are given by the irreducible components of the density matrix[18]

$$\begin{aligned}\rho^{(k)}_q(i\Omega;j) &= (P^{i\Omega}_j)^{-1}\sum_{\omega\omega'}(-1)^{j-\omega}\langle j\omega j-\omega'|kq\rangle\rho^{i\Omega}_{j\omega;j\omega'}(R_b)\\ &= (P^{i\Omega}_j)^{-1}\delta_{q,0}\sum_\omega(-1)^{j-\omega}\langle j\omega j-\omega|k0\rangle P^{i\Omega}_{j\omega}.\end{aligned} \tag{24}$$

We normalized the multipole moments with respect to the population of level j. Note that

$$\begin{aligned}&\rho^{(0)}_0(i\Omega;j) = (2j+1)^{-1/2},\\ &-\frac{2}{\sqrt{6}} \leqslant \rho^{(2)}_0(i\Omega;j=1) \leqslant \frac{1}{\sqrt{6}},\\ &-\frac{2}{\sqrt{14}} \leqslant \rho^{(2)}_0(i\Omega;j=2) \leqslant \frac{2}{\sqrt{14}},\\ &-\frac{4}{\sqrt{70}} \leqslant \rho^{(4)}_0(i\Omega;j=2) \leqslant \frac{6}{\sqrt{70}}.\end{aligned} \tag{25}$$

These normalized multipole moments are related to Zare's molecular frame polarization parameters[19] $A^{(k)}_q$ through

$$\rho^{(k)}_0(j) = \frac{\sqrt{2k+1}[j(j+1)]^{k/2}}{c(k)\langle j||J^{(k)}||j\rangle}A^{(k)}_0. \tag{26}$$

For k up to 4 the reduced matrix elements $\langle j||J^{(k)}||j\rangle$ of the operator equivalents $J^{(k)}$ of order k are listed by Zare,[19] and the normalization constants $c(k)$ are given by Orr–Ewing.[20] General expressions for these quantities are

$$\begin{aligned}\langle j||J^{(k)}||j\rangle &= \sqrt{\frac{(2j+k+1)!(k!)^2}{(2j-k)!2^k(2k)!}},\\ c(k) &= \sqrt{\frac{(2k-1)!!}{k!}}(1+\delta_{k,2}).\end{aligned} \tag{27}$$

The REMPI detection scheme uses a two-photon transition, for which in general the relative absorption intensity is given by[21]

$$I = \sum_k \frac{\tilde{\rho}^{(k)}_0}{\tilde{\rho}^{(0)}_0}I_k(j), \tag{28}$$

where $I_k(j)$ are relative geometrical factors. In the Appendix we derive for the REMPI detection scheme used in the experiment of Buijsse *et al.*[3] that $I_0(j)=1$, $I_2(1) = 2^{-1/2}$, $I_2(2) = -\sqrt{7/10}$, and $I_4(2)=0$. The $\tilde{\rho}^{(k)}_0$ are the $q=0$ multipole moments of the density matrix with respect to the probe frame, i.e., with respect to the polarization axis of the detection laser. Thus, we rotate the multipole moments with respect to the recoil frame to the probe frame by[21]

$$\begin{aligned}\tilde{\rho}^{(k)}_0(i\Omega;j) &= \sum_q \rho^{(k)}_q(i\Omega;j)C_{kq}(\theta,\phi)\\ &= \rho^{(k)}_0(i\Omega;j)P_k(\cos\theta),\end{aligned} \tag{29}$$

where we used $\rho^{(k)}_q = 0$ for $q \neq 0$ and for the Racah normalized spherical harmonics $C_{k0}(\theta,\phi) = P_k(\cos\theta)$.

To obtain the ion images we multiply the angular distribution of the atoms $[1+\beta_{i\Omega}P_2(\cos\theta)]$ with the relative absorption intensity and we weight the contributions of the initial Herzberg states according to the branching ratios $r_{i\Omega}$,

$$\begin{aligned}I^{\rm obs}_j(\theta) = \sum_{i\Omega} r_{i\Omega}[1+\beta_{i\Omega}P_2(\cos\theta)]\\ \times\left\{P^{i\Omega}_j\sum_{k=0}^{2j}\frac{\rho^{(k)}_0(i\Omega;j)}{\rho^{(0)}_0(i\Omega;j)}I_k(j)P_k(\cos\theta)\right\}.\end{aligned} \tag{30}$$

The branching ratios $r_{i\Omega}$ and the anisotropy parameters $\beta_{i\Omega}$ are taken from the experimental papers[3,22] and are summarized in Table II. Note that $r_{i\Omega}$, $\beta_{i\Omega}$, $P^{i\Omega}_j$, and $\rho^{(k)}_0(i\Omega;j)$ all depend on the photodissociation laser wavelength. When we multiply out the two Legendre polynomials in Eq. (30), and re-expand the result in Legendre polynomials, we find the following expression for the ion image:

$$I^{\rm obs}_j(\theta) = \sum_{k=0,2,4} c_k(E,j)P_k(\cos\theta), \tag{31}$$

with

$$\begin{aligned}c_0(E,j) &= \sum_{i\Omega} r_{i\Omega}P^{i\Omega}_j\left\{1+\frac{2}{10}\beta_{i\Omega}\frac{\rho^{(2)}_0(i\Omega;j)}{\rho^{(0)}_0(i\Omega;j)}I_2(j)\right\},\\ c_2(E,j) &= \sum_{i\Omega} r_{i\Omega}P^{i\Omega}_j\left\{\frac{\rho^{(2)}_0(i\Omega;j)}{\rho^{(0)}_0(i\Omega;j)}I_2(j)\right.\\ &\quad\left.+\beta_{i\Omega}\left[1+\frac{2}{7}\frac{\rho^{(2)}_0(i\Omega;j)}{\rho^{(0)}_0(i\Omega;j)}I_2(j)\right]\right\}\\ c_4(E,j) &= \frac{18}{35}\sum_{i\Omega} r_{i\Omega}\beta_{i\Omega}P^{i\Omega}_j\frac{\rho^{(2)}_0(i\Omega;j)}{\rho^{(0)}_0(i\Omega;j)}I_2(j).\end{aligned} \tag{32}$$

Note that Buijsse *et al.* did not attempt to extract the ratio c_4/c_0 from the images. This results in the following intensity ratios for the ion images for $j=0,1,2$:

$$r^{\rm obs}_j(E) = c_0(E,j)\Big/\sum_{j'=0}^{2} c_0(E,j') \tag{33}$$

and anisotropy parameters of the ions

$$\beta^{\rm obs}_j(E) = c_2(E,j)/c_0(E,j). \tag{34}$$

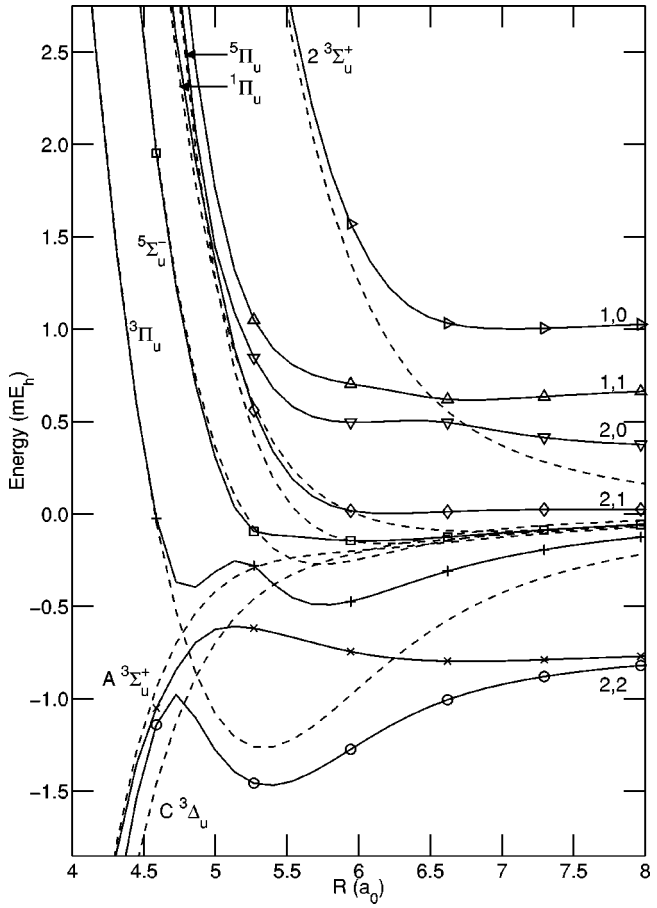

FIG. 1. The ABO potentials (dashed) and the eigenvalues of the total Hamiltonian $\hat{H}(R)$ (solid), for $\Omega=1$. The asymptotic limits are marked j_a, j_b.

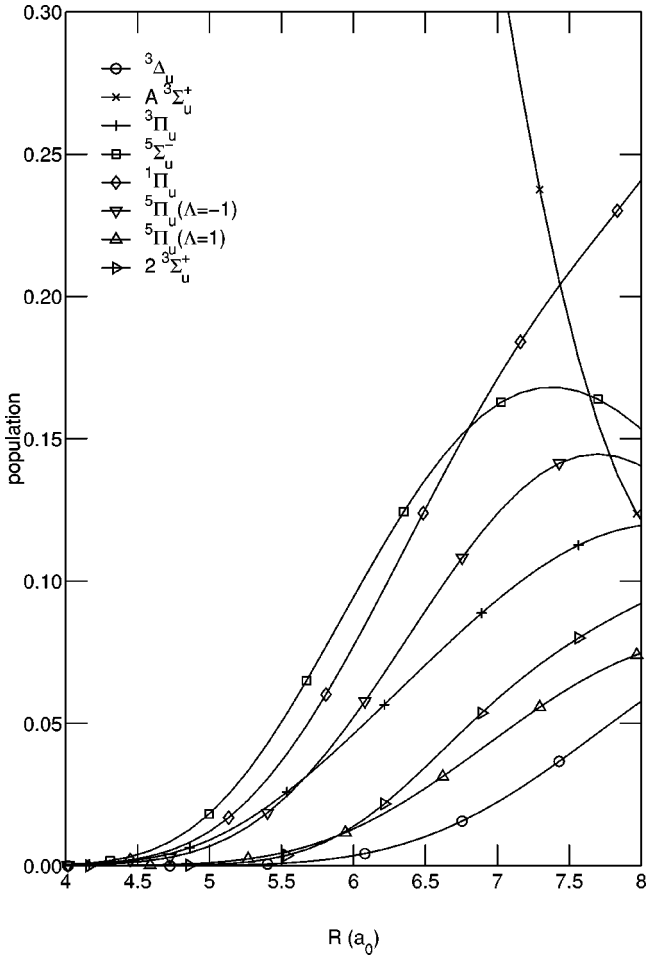

FIG. 2. Populations of the ABO states in the electronic wave function for semiclassical dissociation of initial state $A\ ^3\Sigma_{u,1}^+$, at $\lambda=226$ nm.

The polarization effects on the detection can be seen when we compare intensity ratios to the O(^3P_j) fragment branching ratios

$$r_j(E)=\frac{\Sigma_{i\Omega} r_{i\Omega} P_j^{i\Omega}}{\Sigma_{i\Omega}\Sigma_{j'=0}^{2} r_{i\Omega} P_{j'}^{i\Omega}} \tag{35}$$

and anisotropy parameters

$$\beta_j(E)=\frac{\Sigma_{i\Omega} r_{i\Omega}\beta_{i\Omega} P_j^{i\Omega}}{\Sigma_{i\Omega} r_{i\Omega} P_j^{i\Omega}}. \tag{36}$$

III. RESULTS AND DISCUSSION

Before we present the calculated branching ratios and anisotropy parameters and compare them to the experimental results we will analyze the photodissociation dynamics of the $A\ ^3\Sigma_{u,1}^+$ state in some detail. We select this $\Omega=1$ state because it is the major channel ($\approx 73\%$).

In Fig. 1 we show the ABO potentials $\epsilon_{L|\Lambda|S}(R)$ as well as the Hund's case (c) potentials, i.e., the eigenvalues of the total Hamiltonian $\hat{H}(R)$, for all $\Omega=1$ states. At small R the Coulomb interaction dominates the SO coupling, and the two sets of curves nearly coincide and can be labeled with Hund's case (a) quantum numbers. For large R only the spin–orbit interaction lifts the degeneracy of the states and the Hund's case (c) curves approach the asymptotic values given in Eq. (8) while the ABO potentials all go to zero (with our choice of the zero of energy). Note that the ABO curves, in contrast with the Hund's case (c) curves, may cross when they have the same Ω. The first crossing, around $R=4.75\ a_0$, involves the $A\ ^3\Sigma_{u,1}^+$ and the $^3\Pi_{u,1}$ state.

In Fig. 2 we show the contributions of the ABO states to the electronic wave function as obtained from the semiclassical calculation for the dissociation of the $A\ ^3\Sigma_u^+$ state at 226 nm. For $R<4.5\ a_0$ the wave function remains in the initially excited state. We observe that states that have a nonzero spin–orbit matrix element with the $A\ ^3\Sigma_u^+$ state become populated before the other states [$A'\ ^3\Delta_{u,1}$ and $2\ ^3\Sigma_{u,1}^+$] mix in by a two-step process, as expected. At large R the populations of the ABO states do not reach an asymptotic value, but keep oscillating because the ABO states are not eigenfunctions of $\hat{H}(R)$. In order to analyze at what value of R the fine-structure branching ratios reach their asymptotic value, we plot in Fig. 3 the populations of the asymptotic Hund's case (c) basis functions $|j_a\omega_a j_b\omega_b\rangle_u$. Note that we summed the populations of states with the same (j_a, j_b) quantum numbers. To give an indication of the effect of the photodissociation energy we show curves corresponding to $\lambda=236$ nm (solid lines) and $\lambda=204$ nm (dashed lines). At low energy we see a higher population of states with $(j_a, j_b)=(2,2)$ and a lower population of states yielding $j=0$ frag-

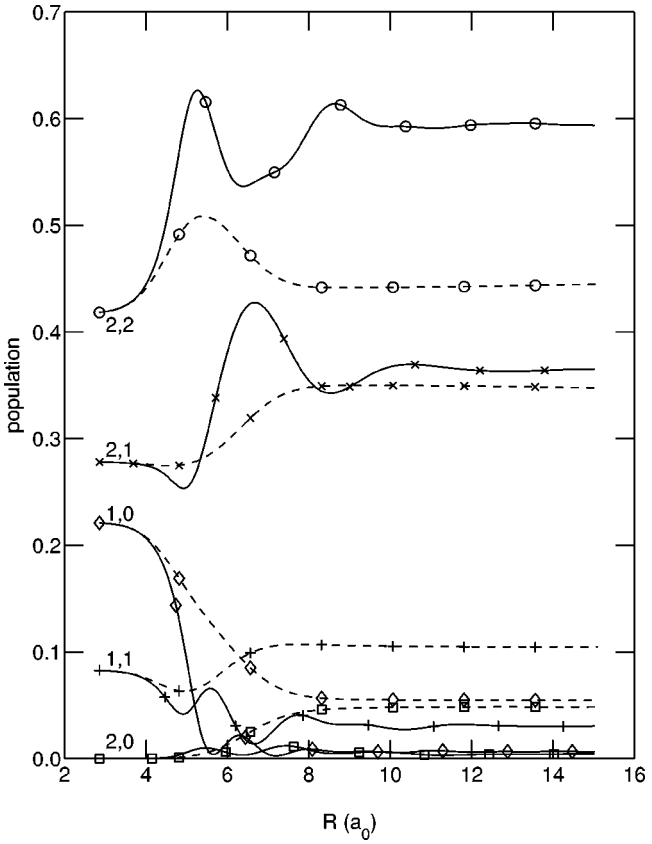

FIG. 3. The electronic wave function for semiclassical dissociation of $A\ ^3\Sigma_{u,1}^+$, at $\lambda=236$ nm (solid lines) and $\lambda=204$ nm (dashed lines). Plotted are populations of asymptotic Hund's case (c) basis functions $|j_a\omega_a j_b\omega_b\rangle_u$, where populations of states with the same j_a, j_b value were added.

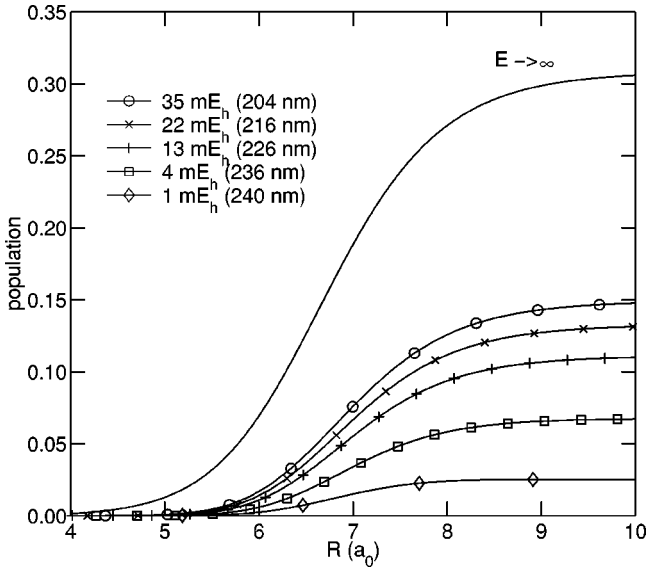

FIG. 4. Population of the $2\ ^3\Sigma_u^+$ ABO basis state ($|(2)01\Sigma;R\rangle$) for dissociation of $A\ ^3\Sigma_u^+$ ($|(0)01\Sigma;R\rangle$) in the extended diabatic model, at different dissociation energies (laser wavelengths).

ments. This is expected since the low energy adiabatic limit predicts purely $j=2$ fragments.

The effect of the nonadiabatic radial derivative coupling is most easily visualized for the extended diabatic model, where it is the *only* coupling. Figure 4 shows how the $2\ ^3\Sigma_u^+$ state is populated as a function of R for a range of photodissociation wavelengths. Although the coupling has its maximum around 6 a_0 (see Fig. 6 in paper I) the transitions mostly occur at somewhat larger R because the energy gap between the $A\ ^3\Sigma_u^+$ and the $2\ ^3\Sigma_u^+$ states is smaller there. The $E\rightarrow\infty$ limit is computed from Eq. (17). Note that at $\lambda=204$ nm, this limit is not yet reached. In the semiclassical calculations the effect of the radial derivative coupling is expected to be less important because spin–orbit coupling reduces the population of the $A\ ^3\Sigma_u^+$ state. Neglecting the radial derivative coupling in the semiclassical calculation changes the fine-structure branching ratios by at most 0.03 and the anisotropy parameters by at most 0.05.

The populations $P_j^{i\Omega}$ and the alignment parameters $\rho_0^{(k)}(i\Omega;j)$ are given in Tables III and IV, respectively, for all Herzberg states separately. Semiclassical results are given for five energies, including the three energies $E=4.325$, 12.87, and 34.61 mE_h, that correspond to the three wavelengths $\lambda=236$, 226, and 204 nm for which experiments were done. We also give the results for the adiabatic model and for the extended diabatic model at $\lambda=204$ nm. Note that for most Herzberg states the semiclassical results for the populations are between the adiabatic and diabatic limits. The exceptions are $A\ ^3\Sigma_{u,0}^+$ and $A'\ ^3\Delta_{u,2}$ states. For the latter state, the $j=2$ population actually has a minimum around $E=6$ mE_h. In the adiabatic model only the $j=2$ state is populated. In the semiclassical calculation for $E=1.108$ mE_h ($\lambda=240$ nm) however only the $c\ ^1\Sigma_{u,0}^-$ and $A'\ ^3\Delta_{u,3}$ have reached a $j=2$ population of more than about 90%, whereas the other states still have substantial contributions for $j<2$. At $E=34.61$ mE_h the populations are generally quite close to the diabatic limit, with the largest absolute difference of 0.13 for the $j=2$ population for the $c\ ^1\Sigma_u^-$ state. Note however that the relative differences with the diabatic limit for the $j=0$ populations can be about a factor of 2, e.g., for the $A\ ^3\Sigma_{u,1}^+$ and $c\ ^1\Sigma_u^-$ states.

By definition $\rho_0^{(0)}(i\Omega;j)=1/\sqrt{2j+1}$ so this parameter is not listed in Table IV. We recall from Sec. II C the ranges for the other parameters: $-0.816\leqslant\rho_0^{(2)}(i\Omega;j=1)\leqslant 0.408$, $-0.535\leqslant\rho_0^{(2)}(i\Omega;j=2)\leqslant 0.535$, and $-0.478\leqslant\rho_0^{(4)}(i\Omega;j=2)\leqslant 0.717$. Note that $\rho_0^{(2)}(A'\ ^3\Delta_{u,3};j=1)$ is equal to its maximum value of 0.408 for all energies. This can be easily understood since a $j_a=1$ atom arising from an $\Omega=3$ state must necessarily have $\omega_a=1$, because $\omega_a+\omega_b=\Omega$ and $|\omega_b|\leqslant 2$. We observe that in general the largest variations in the polarization parameters occur for low energies. The atomic polarizations have not yet been measured directly. Experimental determination of these parameters would be a welcome extra test of the present calculations. We only list the $\rho_0^{(4)}(i\Omega;j)$ parameters for completeness, they do not play a role in the present two-photon detection scheme.

We compute the fine-structure branching ratios for the photodissociation of O_2 $[r_j(E)]$ by combining the branching ratios for excitation of the different Herzberg states ($r_{i\Omega}$) given in Table II with the population parameters $P_j^{i\Omega}$ according to Eq. (35). The energy dependent results for the semiclassical as well as the extended diabatic calculations are shown in Fig. 5. The intensity ratios that may be determined

TABLE III. Populations $P_j^{i\Omega}(E)$ for the extended diabatic model at the highest energy (34.61 mE_h), for the semiclassical calculation at several energies, and for the adiabatic limit, which is not energy dependent.

			Semiclassical					Diabatic
State	j	Adiabatic	E=1.108 λ=240	4.325 236	12.87 226	22.20 216	34.61 204	34.61 mE_h 204 nm
$A\ ^3\Sigma^+_{u,1}$	2	1	0.778	0.744	0.692	0.663	0.642	0.547
	1	0	0.216	0.240	0.273	0.292	0.306	0.359
	0	0	0.005	0.016	0.035	0.045	0.052	0.094
$A\ ^3\Sigma^+_{u,0^-}$	2	1	0.591	0.557	0.490	0.472	0.472	0.573
	1	0	0.369	0.330	0.337	0.339	0.335	0.282
	0	0	0.040	0.113	0.173	0.189	0.193	0.145
$c\ ^1\Sigma^-_{u,0^-}$	2	1	0.948	0.899	0.820	0.771	0.732	0.593
	1	0	0.051	0.095	0.159	0.196	0.223	0.311
	0	0	0.001	0.005	0.021	0.033	0.045	0.096
$A'\ ^3\Delta_{u,1}$	2	1	0.640	0.538	0.439	0.405	0.385	0.334
	1	0	0.337	0.404	0.468	0.485	0.493	0.500
	0	0	0.023	0.058	0.092	0.110	0.122	0.166
$A'\ ^3\Delta_{u,2}$	2	1	0.552	0.532	0.549	0.559	0.567	0.584
	1	0	0.365	0.334	0.281	0.266	0.258	0.250
	0	0	0.083	0.134	0.170	0.175	0.175	0.166
$A'\ ^3\Delta_{u,3}$	2	1	0.896	0.842	0.807	0.795	0.788	0.751
	1	0	0.104	0.158	0.193	0.205	0.212	0.249
	0	0	0	0	0	0	0	0

from the ion images formally depend on the polarization of the atoms according to Eq. (33). In Fig. 5 we see that only for the lowest energy in the semiclassical calculation there is a small difference between the intensity ratios in the images (solid lines) and the branching ratios (dashed lines). Experimentally determined intensity ratios are only available for λ=226 nm. We find that the semiclassical results lie within the experimental error bars, while the extended diabatic

TABLE IV. Alignment parameters $\rho_0^{(k)}(i\Omega;j)(E)$ for the extended diabatic model at the highest energy (34.61 mE_h), for the semiclassical calculation at several energies, and for the adiabatic limit, which is not energy dependent. The parameters with k=0 are $1/\sqrt{2j+1}$ by definition, those are not listed.

			Semiclassical					Diabatic
State	(j,k)	Adiabatic	E=1.108	4.325	12.87	22.20	34.61	34.61 mE_h
$A\ ^3\Sigma^+_{u,1}$	(1,2)		−0.272	0.083	0.095	0.068	0.047	0.037
	(2,2)	−0.3859	−0.282	−0.153	−0.073	−0.041	−0.021	0.013
	(2,4)	0.1111	0.033	0.049	0.010	−0.014	−0.033	−0.067
$A\ ^3\Sigma^+_{u,0^-}$	(1,2)		0.122	−0.214	−0.498	−0.569	−0.610	−0.538
	(2,2)	0.3129	0.094	0.137	0.189	0.219	0.243	0.309
	(2,4)	−0.0457	−0.099	−0.039	0.078	0.127	0.153	0.128
$c\ ^1\Sigma^-_{u,0^-}$	(1,2)		0.195	0.212	0.165	0.113	0.060	−0.162
	(2,2)	−0.0457	0.072	0.171	0.225	0.242	0.252	0.221
	(2,4)	−0.3129	−0.213	−0.136	−0.093	−0.074	−0.057	−0.000
$A'\ ^3\Delta_{u,1}$	(1,2)		−0.244	−0.194	−0.198	−0.201	−0.202	−0.205
	(2,2)	0.1186	−0.096	−0.167	−0.227	−0.310	−0.327	−0.334
	(2,4)	−0.1709	−0.088	−0.061	−0.055	−0.069	−0.086	−0.178
$A'\ ^3\Delta_{u,2}$	(1,2)		−0.307	−0.424	−0.638	−0.719	−0.762	−0.816
	(2,2)	0.000	0.214	0.309	0.380	0.391	0.392	0.381
	(2,4)	0.4183	0.012	0.035	0.128	0.160	0.178	0.205
$A'\ ^3\Delta_{u,3}$	(1,2)		0.408	0.408	0.408	0.408	0.408	0.408
	(2,2)	0.1336	0.180	0.209	0.230	0.237	0.242	0.266
	(2,4)	−0.1793	−0.145	−0.123	−0.108	−0.102	−0.099	−0.080

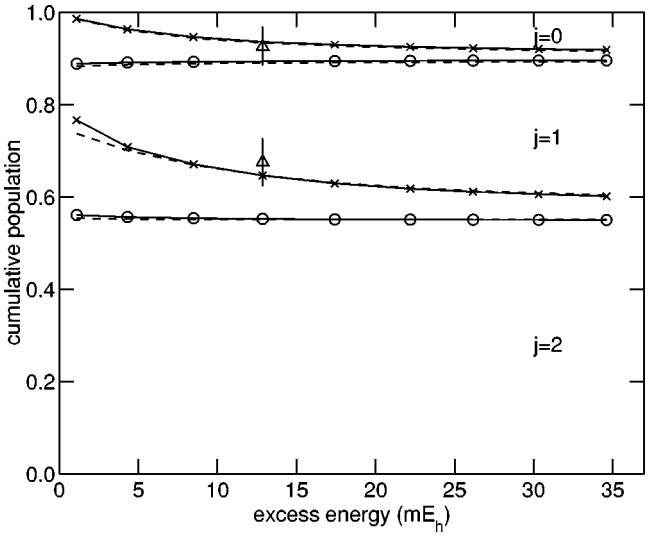

FIG. 5. Cumulative plot of distribution over atomic j levels. The diabatic model is marked ○. The experimental data are given with △ marks and error bars. The semiclassical results are marked ×. The dashed lines represent the fine-structure branching ratios r_j, the solid lines represent the intensity ratios of the ion images, $r_j^{\mathrm{obs}}(E)$.

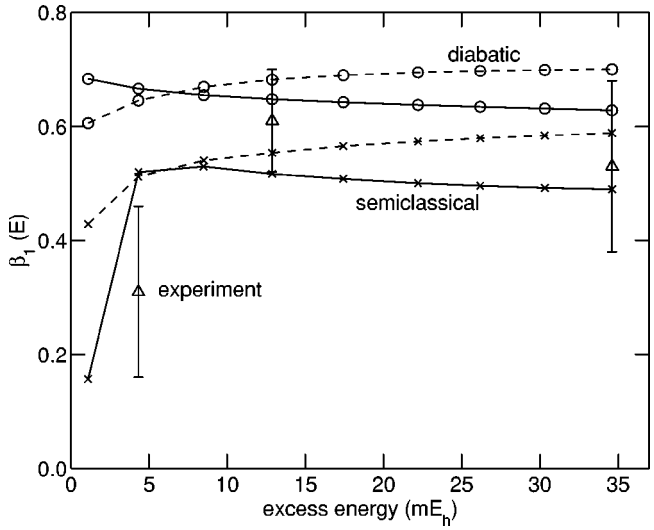

FIG. 7. The parameters $\beta_1(E)$ (dashed) and $\beta_1^{\mathrm{obs}}(E)$ (solid). The semiclassical calculation is marked ×, the diabatic model results are marked ○, and the experiment is marked with △ and error bars.

model is clearly outside the error bars. Note that the semiclassical results are between the adiabatic (100% $j=2$) and diabatic limits for the full energy range considered.

In Figs. 6, 7, and 8 we compare the calculated anisotropy parameters with experiment for, respectively, $j=0$, 1, and 2 atomic fragments. For $j=1$ and $j=2$ polarization of the atoms may cause a difference between the anisotropy of the atomic fragment distribution [$\beta_j(E)$, the dashed lines in the figures] and the experimentally determined anisotropy parameters $\beta_j^{\mathrm{obs}}(E)$ of the ion images (solid lines in the figures). Note that the largest polarization effects are predicted for low energies. For $j=2$ and $j=1$ the semiclassical results are in better agreement with experiment than the extended diabatic model. For $j=2$ we also have results for the adiabatic model. For this model we find a large polarization effect, just as for the semiclassical calculations at low energy. The largest deviations between the semiclassical calculation and experiment occur for $j=0$ (Fig. 6). This is somewhat surprising since in this case there are no polarization effects, so the branching ratios determine the anisotropy parameters. However, in Fig. 5 we already saw that the semiclassical results are in good agreement with the experimentally determined branching ratios at $\lambda=226$ nm. Clearly, additional independent experimental data on the branching ratios and anisotropy parameters would be most welcome to further test our understanding of the photodissociation dynamics of O_2 in the Herzberg continuum. Furthermore, note that we took the Herzberg excitation branching ratios and anisotropy parameters from the experimental paper.[3] These values were determined from extrapolation of spectroscopic data. However, the R dependence of the transition moments that was

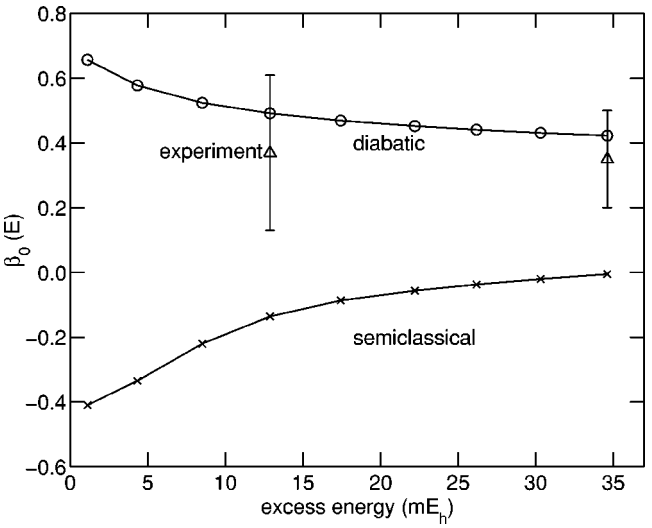

FIG. 6. The anisotropy parameter $\beta_0(E)$. The markers have the same meaning as in Fig 5.

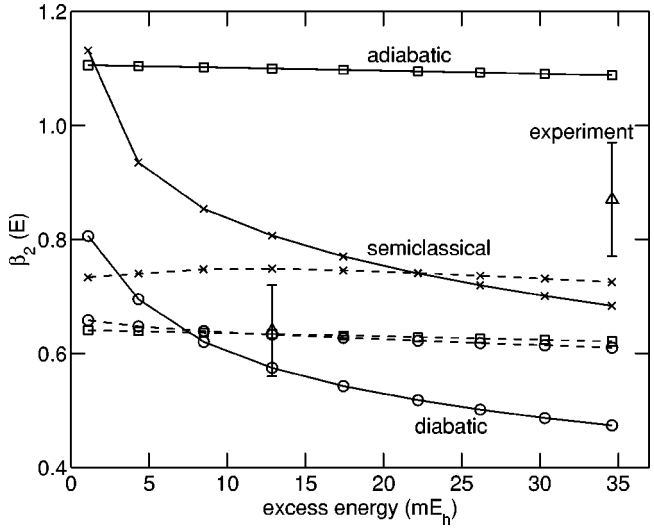

FIG. 8. The parameters $\beta_2(E)$ and $\beta_2^{\mathrm{obs}}(E)$. The adiabatic model results are marked with squares, the other markers have the same meaning as in Fig 7.

used in the excitation model in Ref. 3 is not in full agreement with *ab initio* calculations.[23,3]

IV. CONCLUSION

Several electronic states contribute to the photodissociation of O_2 in the Herzberg continuum. The photodissociation dynamics determines the fine-structure branching ratios for these states. This is reflected in the anisotropy of the fine-structure resolved fragment distributions. In paper I we computed potentials, spin–orbit and radial derivative couplings for electronic wave functions that were carefully constructed to have the correct long range behavior. In this paper we present the results of semiclassical dynamics calculations, which apply these potentials and couplings. We compare the calculated branching ratios and anisotropy parameters to experimental results. In order to investigate the adiabaticity of the dissociation we also present results for the limiting adiabatic and diabatic models.

We find that at the lowest energy for which experimental data ($\lambda = 236$ nm) are available the dynamics is still not fully adiabatic and at the highest energy ($\lambda = 204$ nm) it is not yet fully diabatic. The dynamics is mainly determined by transitions that occur between 4.5 and 9 a_0, where the spin–orbit interaction becomes large compared to the separation of the ABO potentials. We also considered the effect of the radial derivative coupling between the $A\ ^3\Sigma_u^+$ and $2\ ^3\Sigma_u^+$ states. In the hypothetical infinite energy limit this coupling causes a $2\ ^3\Sigma_u^+$ population of about 30%. In the extended diabatic limit we ignore the SO coupling and only include the radial derivative coupling. We find that for $\lambda = 204$ nm the $2\ ^3\Sigma_u^+$ state is still only populated by about 15%. In the semiclassical calculations the $A\ ^3\Sigma_u^+$ state becomes (partly) depopulated through spin–orbit coupling before the radial derivative coupling reaches its maximum, hence the effect on the calculated images is small.

The 2+1 REMPI detection used in the experiment is sensitive to the polarization of the atoms. The semiclassical calculations show that strong polarization effects on the anisotropy of the ion images can be expected for low energies. Formally, polarization of the atoms also affects the determination of the fine-structure branching ratios from the ion images, but we find that this effect is almost negligible.

Generally, there is reasonable agreement between the semiclassical calculations and experiment. The largest difference between the semiclassical calculations and experiment occurs for the anisotropies in the $j = 0$ images. In the present study we took the Herzberg excitation branching ratios from literature results which mainly rely on experimental data. We believe that additional *ab initio* calculations of the transition moments may help to resolve the remaining differences. Also, experimental determination of the anisotropy parameters with smaller error bars and a direct determination of the polarization of the atoms, particularly at low energies would be most welcome.

ACKNOWLEDGMENTS

The authors thank Ad van der Avoird and Paul E. S. Wormer for useful discussions and for carefully reading the paper. This research has been financially supported by the Council for Chemical Sciences of the Netherlands Organization for Scientific Research (CW–NWO).

APPENDIX: DERIVATION OF DETECTION ANGULAR SENSITIVITY

The geometrical factors $I_k(j)$ for the REMPI detection are derived from the spherical components of the two-photon excitation intensity operator. Following Ref. 24 we write the $q = 0$ spherical components of the geometrical factors of a general two-photon transition in the case of linearly polarized light as

$$I_k^{\mathrm{SF}}(j_i,j_f) = \sum_m (-1)^{j_i-m}\sqrt{2k+1}\begin{pmatrix} j_i & k & j_i \\ -m & 0 & m \end{pmatrix} \times \left| \sum_{j_e} (-1)^{j_f+j_e}\begin{pmatrix} j_f & 1 & j_e \\ -m & 0 & m \end{pmatrix} \times \begin{pmatrix} j_e & 1 & j_i \\ -m & 0 & m \end{pmatrix} R(j_e) \right|^2, \tag{A1}$$

where

$$R(j_e) = \sum_{n_e} \frac{\langle n_f j_f || r^{(1)} || n_e j_e \rangle \langle n_e j_e || r^{(1)} || n_i j_i \rangle}{E_{n_e} - E_{n_i} - h\nu + i(\Gamma_e/2)}. \tag{A2}$$

The transition is from initial state $|n_i j_i m\rangle$ to final state $|n_f j_f m\rangle$, through intermediate states $|n_e j_e m\rangle$, where j_i, j_e, j_f denote the total angular momentum, m denotes the projection of the angular momentum on the space fixed (SF) axis of laser polarization, and n_i, n_e, n_f denote all other quantum numbers of initial, intermediate, and final state, respectively. The symbols $\langle n_f j_f || r^{(1)} || n_e j_e \rangle$ and $\langle n_e j_e || r^{(1)} || n_i j_i \rangle$ represent the reduced matrix elements of the transition dipole $r_m^{(1)}$, E_{n_e}, and E_{n_i} are the energies of intermediate and initial state, ν is the frequency of the detection laser, and Γ_e is the homogeneous linewidth. The factors $I_k^{\mathrm{SF}}(j_i,j_f)$ are called P_k by Mo *et al.* Components with $q \neq 0$ are zero for a two-photon absorption process.

Experiments[25] and theoretical calculations[26] have shown that the intermediate state $2s^2 2p^3 3s\, ^3S^0$ contributes about 97% of the total two-photon excitation line strength in the (2+1) REMPI detection of $O(^3P_j)$ at 226 nm. When we neglect possible other intermediate states, the only possible value for j_e equals 1, and the summation over n_e drops out of the reduced matrix element factor $R(j_e)$. Then $R(j_e)$ is the same for all components of one transition $|n_f j_f\rangle \leftarrow |n_i j_i\rangle$. Since we are only interested in relative intensities, this factor can be divided out. We find

$$I_k^{\mathrm{SF}}(j_i,j_f) = \sum_m (-1)^{j_i-m}\sqrt{2k+1}\begin{pmatrix} j_i & k & j_i \\ -m & 0 & m \end{pmatrix} \times \begin{pmatrix} j_f & 1 & j_e \\ -m & 0 & m \end{pmatrix}^2 \begin{pmatrix} j_e & 1 & j_i \\ -m & 0 & m \end{pmatrix}^2. \tag{A3}$$

In the experiment, the final state is not resolved, and we have to sum over all possible final states. Using the single-intermediate-state model the branching ratios $r^{\mathrm{at}}(j_f \leftarrow j_i)$

TABLE V. Branching ratios $r^{at}(j_f \leftarrow j_i)$ for the REMPI transition $O(2p^3(^4S)3p\ ^3P_{j_f}) \leftarrow O(2p^4\ ^3P_{j_i})$ via the $2p^3 3s^3S^0$ intermediate state.

j_i	j_f	$r^{at}(j_f \leftarrow j_i)$
0	0	1/3
0	1	0
0	2	2/3
1	0	0
1	1	1/2
1	2	1/2
2	0	2/15
2	1	3/10
2	2	17/30

from one given j_i to the three possible final states j_f are also given by Bischel.[25] These values are given in Table V. We then finally find

$$I_k(j) = \sum_{j_f=0}^{2} r^{at}(j_f \leftarrow j) I_k^{SF}(j, j_f) / I_0^{SF}(j, j_f). \tag{A4}$$

[1] H. M. Lambert, P. J. Dagdigian, and M. H. Alexander, J. Chem. Phys. **108**, 4460 (1998).
[2] G. Parlant and D. R. Yarkony, J. Chem. Phys. **110**, 363 (1999).
[3] B. Buijsse, W. J. van der Zande, A. T. J. B. Eppink, D. H. Parker, B. R. Lewis, and S. T. Gibson, J. Chem. Phys. **108**, 7229 (1998).
[4] A. T. J. B. Eppink and D. H. Parker, Rev. Sci. Instrum. **68**, 3477 (1997).
[5] M. C. G. N. van Vroonhoven and G. C. Groenenboom, J. Chem. Phys. **116**, 1954 (2002), preceding paper.
[6] S. J. Singer, K. F. Freed, and Y. B. Band, Adv. Chem. Phys. **61**, 1 (1985).
[7] Y.-L. Huang and R. J. Gordon, J. Chem. Phys. **94**, 2640 (1991).
[8] B. Zygelman, A. Dalgarno, and R. D. Sharma, Phys. Rev. A **49**, 2587 (1994).
[9] S. J. Singer, K. F. Freed, and Y. B. Band, J. Chem. Phys. **79**, 6060 (1983).
[10] J. B. Delos, Rev. Mod. Phys. **53**, 287 (1981).
[11] C. E. Moore, *Atomic Energy Levels as Derived from the Analysis of Optical Spectra*, Vol. I, No. 35, National Sandards Reference Data Series (National Bureau of Standards, Washington, DC, 1971).
[12] J. B. Delos, W. R. Thorson, and S. K. Knudson, Phys. Rev. A **6**, 709 (1972).
[13] J. B. Delos and W. R. Thorson, Phys. Rev. A **6**, 720 (1972).
[14] P. C. Cosby and D. L. Huestis, J. Chem. Phys. **97**, 6108 (1992).
[15] The MATLAB computer linear algebra system is available from The Mathworks, Inc., accessible online at http://www.mathworks.com/
[16] C. H. Greene and R. N. Zare, Annu. Rev. Phys. Chem. **33**, 119 (1982).
[17] L. D. A. Siebeles, M. Glass-Maujean, O. S. Vasyutinskii, J. A. Beswick, and O. Roncero, J. Chem. Phys. **100**, 3610 (1994).
[18] K. Blum, *Density Matrix Theory and Applications*, Physics of atoms and molecules series (Plenum, New York and London, 1981), Chap. 4 deals with the irreducible components of the density matrix.
[19] R. N. Zare, *Angular Momentum* (Wiley, New York, 1988).
[20] A. J. Orr-Ewing and R. N. Zare, Annu. Rev. Phys. Chem. **45**, 315 (1994).
[21] Y. Mo and T. Suzuki, J. Chem. Phys. **109**, 4691 (1998).
[22] C. M. L. Kerr and J. K. G. Watson, Can. J. Phys. **64**, 36 (1986).
[23] R. Klotz and S. D. Peyerimhoff, Mol. Phys. **57**, 573 (1986).
[24] Y. Mo, H. Katayanagi, M. C. Heaven, and T. Suzuki, Phys. Rev. Lett. **77**, 830 (1996).
[25] W. K. Bischel, B. E. Perry, and D. R. Crosley, Appl. Opt. **21**, 1419 (1982).
[26] M. S. Pindzola, Phys. Rev. A **17**, 1021 (1978).